Dalton Transactions

Accepted Manuscript

ROYAL SOCIETY OF CHEMISTRY

www.rsc.org/dalton

Influence of spherical assembly of copper ferrite nanoparticles on magnetic properties: Orientation of magnetic easy axis†

Biplab K. Chatterjee [a], Kaustav Bhattacharjee [b], Abhishek Dey [a], Chandan K. Ghosh [a] and Kalyan K. Chattopadhyay [a, c,*]

[a] *School of Materials Science and Nanotechnology, Jadavpur University, Jadavpur, Kolkata-700032, India*

[b] *Metallurgical and Material Engineering, Jadavpur University, Jadavpur, Kolkata-700032, India*

[c] *Thin Film and Nanoscience Laboratory, Department of Physics, Jadavpur University, Jadavpur, Kolkata-700032, India*

*Corresponding e-mail: kalyan_chattopadhyay@yahoo.com; FAX: 91 33 24146007

†Electronic supplementary information (ESI) available: Atomic absorption spectroscopy (AAS) analysis (Table S1), X-ray diffraction analysis, Magnetic property analysis (orientation of magnetic easy axis)

Abstract

The magnetic property of copper ferrite ($CuFe_2O_4$) nanoparticles prepared via sol-gel auto combustion and facile solvothermal method are studied focusing on the effect of nanoparticles arrangement. Randomly oriented $CuFe_2O_4$ nanoparticles (NP) are obtained from the sol-gel auto combustion method while, the solvothermal method allows us to prepare iso-oriented uniform spherical ensembles of $CuFe_2O_4$ nanoparticles (NS). X-ray diffractometer (XRD), atomic absorption spectroscopy (AAS), infra-red (IR) spectroscopy, Raman spectroscopy, scanning electron microscopy (SEM), transmission electron microscopy (TEM), ^{57}Fe Mössbauer spectroscopy and vibrating sample magnetometer (VSM) are used to investigate the composition, microstructure and magnetic properties of as-prepared ferrite nanoparticles. The field-dependent magnetization measurement for NS sample at low temperature exhibits step-like rectangular hysteresis loop ($M_R/M_S \sim 1$) suggesting cubic anisotropy in the system, whereas for NP sample, typical features of uniaxial anisotropy ($M_R/M_S \sim 0.5$) is observed. The coercieve field (H_C) for NS sample shows anomalous temperature dependence, which is correlated with the variation of effective anisotropy (K_E) of the system. A high-temperature enhancement of H_C and K_E for NS sample coincides with a strong spin-orbit coupling in the sample as evidenced by a significant modification of Cu/Fe-O bond distances. The spherical arrangement of the nanocrystals at the mesoscopic scale provokes a high degree of alignment of magnetic easy axis along the applied

field leading to step-like rectangular hysteresis loop. A detailed study on the temperature dependence of magnetic anisotropy of the system is carried out, emphasizing the influence of the formation of spherical iso-oriented assemblies.

Key words: copper ferrite, magnetic anisotropy, coercivity, nanoparticles arrangement, orientation easy axis

Introduction

The magnetic features of nanoscale material are immensely susceptible to the dimension of crystalline coherent domains (*i.e.*, crystallite) due to finite size effect as well as surface effect, which become extremely significant as the particle size get reduced.[1, 2] The energy of a single domain particle with uniaxial anisotropy usually depends on the magnetization direction, and when φ is the angle between the magnetization vector and the direction of external field (H), it can be described as[3, 4]

$$U = K_E V \sin^2\theta - \mu V H \cos\varphi \qquad (1)$$

where K_E is the effective anisotropy, V is the particle volume, μ is the magnetic moment and, θ is the angle between easy direction and magnetic moment. According to the Neel-Brown theory of superparamagnetism[5, 6], the magnetic behavior of a nanoparticle can be described by a certain temperature (the blocking temperature, T_B) on a certain time scale. Above T_B, with adequate thermal energy, the particle moment can generate a thermally activated superparamagnetic transition. Bellow T_B, the moment is blocked and unable to overcome the anisotropy barrier in the time of a measurement.[7]

The anisotropy energy of the nanoparticle not only depends on the dimension of the particle (V) and anisotropy constant (K_E) of the system, but essentially on the orientation of magnetic easy axis with respect to the field direction as described by equation 1.[3] The crystal symmetry and chemical composition of a nanoscale material varies significantly with a minor change in synthesis conditions, which leads to instability in effective anisotropy constant (K_E) of the material. Therefore, the tailoring of magnetic property of nanoparticles (*e.g.*, coercivity, remanence, blocking temperature) is possible by means of control over the anisotropy energy of nanoparticles by varying the synthesis conditions.

For an ensemble of nanoparticles, in which the nanoparticles are arranged in a definite order or randomly oriented, the magnetic properties are hugely influenced by interparticle interactions that can be magnetic dipole-dipole or exchange coupling between the surface atoms of the adjacent particles. The nature and strength of interparticle interactions depend on the "arrangement" of nanoparticles.[8]

Over the past few decades, tremendous attention has been given on nanoscale ferrite materials. These materials are generating huge interest because of their potential for elucidating fundamental nanomagnetism and technological applications in diverse fields. Spinel ferrites, especially nanostructured copper ferrite ($CuFe_2O_4$) exhibit interesting magnetic, magneto-resistive and magneto-optical properties and finds potential application in high-density magneto-optic recording devices[9], magnetic resonance imaging (MRI)[10], magnetic refrigeration[11], magnetic bulk cores, ferrofluids[12], microwave absorbers[13], medical diagnostics[14], catalytic uses[15] *etc*.

Copper ferrite ($CuFe_2O_4$) is a soft material having low coercieve field and saturation magnetization with high electrical resistance which leads to very low eddy current losses.[16] It

crystallizes in two different phases (*e.g.*, cubic and tetragonal) depending upon the cation distribution in tetrahedral (A) and octahedral (B) sites.[17, 18] Cubic structure of spinel $CuFe_2O_4$ is described as a close-packed arrangement of O^{2-} ions with Cu^{2+} and Fe^{3+} ions at tetrahedral (A) and octahedral (B) crystallographic sites.[19] The presence of Cu^{2+} ions at octahedral environment with orbitally degenerate ground state (d^9 electronic configuration) in $CuFe_2O_4$ spinel structure may lead to Jahn-Teller distortion (c/a > 1) modifying the local symmetry of the sites.[20] A whole range of cation distribution is possible in this type of structures which can be described as

$$[Cu^{2+}_{x}Fe^{3+}_{1-x}]^{A}[Cu^{2+}_{1-x}Fe^{3+}_{1+x}]^{B}O^{2-}_{4}$$

where $x = 0$ and $x = 1$ stand for inverse and normal cases, respectively. The degree of inversion (x) depends on the synthesis technique, thermal treatment and size of cations. The alteration of the degree of inversion (x) up to a certain limit modifies the structure and size of tetrahedral and octahedral polyhedra without changing the overall symmetry ($Fd\bar{3}m$) of cubic spinel lattice. Therefore, the tetrahedral and octahedral polyhedra are slightly deformed, which is enumerated by the change in oxygen positional parameter (u) and lattice constant (a) of the lattice; consequently the metal-oxygen bond distances are also modified. The origin of magnetic properties of spinel ferrite is the spin magnetic moment of unpaired transition metal 3d electrons coupled by the superexchange interaction via oxygen ions separating them.[21] The modification in bond distances significantly alters the strength of A-O-B (J_{AB}), A-O-A (J_{AA}) and B-O-B (J_{BB}) superexchange interactions and these competing interactions among the A and B sublattices may lead to topological frustration, yielding a magnetic structure that may include states of antiferromagnetic order, local spin canting, spin-glass-like behavior, disordered phases, and ferrimagnetic order.[21] Therefore, the variation of metal ion contents at tetrahedral (A) and octahedral (B) sites along with the finite-size effect, large surface contribution and interparticle

interaction causes diverse anomalous behavior in magnetic ferrite nanomaterials which are in huge discussion.

A large number of synthetic strategies, such as normal and reverse micelle[22, 23], co-precipitation[24], mechanical milling[25], sonochemistry, aerosol vapor method, surfactant assisted high-temperature decomposition[26], combustion method[27] and hydrothermal processing[28, 29] have been suitably proposed to fabricate new magnetic nanostructured ferrites. Normal and reverse micelle methods have been used to synthesize a wide range of ferrite nanoparticles with different shape and size and with narrow particle size distribution.[30] Despite the high number of advantages of miceller method, because of the low synthesis temperature, a poor degree of crystallinity is often observed. In the 20th century, a further progress in the control of size and morphology of crystallites, microstructural features, crystallinity and significantly reduced aggregation levels combined with narrow size distribution of nanoparticles has been given by hydrothermal techniques.[31] Although, a lot of work has been performed on each synthesis method, detail comparison between nanomaterials prepared via different synthesis method is still lacking. In this frame, the intention of the present work is to compare the morpho-structural and magnetic properties of copper ferrite ($CuFe_2O_4$) nanoparticles prepared via the sol-gel auto combustion and solvothermal method, investigating their prospective in altering the nanoparticles arrangement. The sol-gel auto combustion method consents us to achieve randomly oriented $CuFe_2O_4$ crystalline nanoparticles (NP). On the other hand, the solvothermal method results to be appropriate to synthesize spherical iso-oriented assembly of nanoparticles (NS). Using these methods, the present work aims to shed light on the influence of synthesis method and "arrangement" of nanoparticles on the magnetic property of as-prepared $CuFe_2O_4$ samples. In addition, specific interest is given to the temperature dependence of effective anisotropy

constant (K_E) of the system and orientation of the anisotropy easy axis, emphasizing the role of the formation of spherical iso-oriented assemblies.

Experimental

Chemicals

Ferric chloride hexahydrate ($FeCl_3 \cdot 6H_2O$), copper chloride dihydrate ($CuCl_2 \cdot 2H_2O$), ferric nitrate nonahydrate ($Fe(NO_3)_3 \cdot 9H_2O$), copper nitrate trihydrate ($Cu(NO_3)_2 \cdot 3H_2O$), ammonium acetate, ethylene glycol (EG), polyethylene glycol (PEG), hydrated citric acid and ethylenediamine (EDA) are obtained from Sigma-Aldrich. All chemicals are of analytical grade and used without further purification. Triply distilled deionized water obtained from Milli-Q water purification system (Millipore) is used throughout the experiment.

Synthesis of randomly distributed copper ferrite nanoparticles (NP)

10 mmol of $Cu(NO_3)_2 \cdot 3H_2O$, 20 mmol of $Fe(NO_3)_3 \cdot 9H_2O$ are taken in a beaker and hydrated citric acid (5.6476 g) of the combined equivalent weight of the salts is added into the mixture. A saturated solution is prepared by adding minimum amount of deionized water into the mixture and continuously stirred to avoid precipitation. EDA is added drop by drop into the solution until pH of the solution reached 5. The citrate ions present in the solution helped in the formation of the gel. The gel is dried thoroughly by heating it in an oven at 80 °C for about 18 h. A uniformly colored green transparent glassy material containing the cations homogeneously mixed on an

atomic scale is formed. This glassy material is then heated in a furnace for 2 h at 200°C and a fluffy blackish brown mass containing nanocrystalline $CuFe_2O_4$ nanoparticles is obtained.

Synthesis of uniform spherical assembly of copper ferrite nanoparticles (NS)

5 mmol of $FeCl_3 \cdot 6H_2O$ and 2.5 mmol of $CuCl_2 \cdot 2H_2O$ are dissolved in 50 mL of ethylene glycol (EG) and 0.8 mL of polyethylene glycol (PEG) in a beaker under magnetic stirring. After 45 min, 20 mmol of ammonium acetate is added to the previous solution with vigorous stirring. After continuous stirring for another 120 min, the obtained homogeneous dark green solution is transferred into a Teflon-lined stainless-steel autoclave (65 mL volume) and sealed. The autoclave is then placed in an oven at a temperature 180^{o}C for a solvothermal reaction. After a 24 h reaction period, the autoclave is cooled to room temperature. The solution is then filtered to get dark precipitate. The precipitate is washed repeatedly by distilled water and ethyl alcohol alternatively and dried at room temperature for 48-72 h. The collected sample is taken for further characterization.

Characterization

The crystallinity, crystal structure and phase purity of the powder sample are investigated by making use of the X-ray diffraction technique at room temperature using Cu-K_α radiation of wavelength 1.5404 Å, in steps of 0.02^o and step count time of 3 s on a Rigaku Ultima-III x-ray diffractometer (Bragg-Brentano geometry). We adopted Rietveld's powder structure refinement analysis[32-35] of x-ray powder diffraction step scan data by using the JAVA based software program MAUD[36] to obtain the structural and microstructural refinement parameters through a least-square method. The experimental profiles are fitted with the most suitable pseudo-Voigt

(pV) analytical function[34] with asymmetry and the background of each pattern is fitted with a fourth order polynomial function.

Atomic absorption spectroscopy (AAS) studies are carried out on a Perkin Elmer Analyst 200 flame atomic absorption spectrometer to determine the concentration of metal ions (Cu^{2+}, Fe^{3+}) in the synthesized samples and thereby to ascertain the stoichiometry of the samples. Fresh samples are completely dissolved in concentrated HCl and diluted to a known volume in volumetric flasks prior to AAS analysis.

Infra-red (IR) spectra are taken on an IR-Prestige, Shimadzu spectrometer using KBr pellets in the range between 400 and 1200 cm^{-1}. Raman spectra in the range from 100 to 800 cm^{-1} are recorded at room temperature using a confocal Raman imaging system (WITec GmbH) alpha 300RS. The UHTS 300 spectrograph is connected with a Peltier-cooled back-illuminated CCD camera with better than 90% QE in the visible excitation. A laser radiation source operating at a wavelength of 532 nm and a power of 40 mW is used.

The samples are observed in electron micrographs obtained with a TEM system (JEOL) operating at 200 kV. Finely ground samples are dispersed in ethanol and submitted to an ultrasonic bath and the suspensions are then dropped on carbon-coated copper grids. The average particle size is obtained using bright-field images measuring the average diameter on over 100 particles in different parts of the grid. High resolution transmission electron microscope (HRTEM) images are obtained to confirm the nanocrystalline nature of the as-prepared samples. The shape and surface morphology of the samples are determined using a field emission scanning electron microscope (FESEM, Hitachi S-4800).

^{57}Fe Mössbauer spectra are recorded in transmission mode with a ^{57}Co(Rh) source and in constant acceleration mode for the two samples at room temperature. The instrument is calibrated using a natural iron foil. The Mössbauer spectra of the samples are fitted using the program package NORMOS.[37]

The dc magnetic measurements are performed using VSM technique by Physical Property Measurement System (PPMS, Cryogen, UK). Magnetization versus temperature measurements are carried out using zero-field-cooled (ZFC) and field-cooled (FC) protocols. $M_{FC}(T)$ and $M_{ZFC}(T)$ measurements are performed by cooling the sample from room temperature to 5 K under zero magnetic field; then, a static magnetic field of 100 Oe is applied. $M_{ZFC}(T)$ is measured during the warming cycle from 5 K to 300 K, whereas $M_{FC}(T)$ is recorded during the subsequent cooling under zero magnetic field. The field dependent hysteresis curves are recorded at different temperatures between 5 K and 300 K by varying the field in the range ± 3.5 T.

Results and Discussion

Chemical composition analysis by atomic absorption spectroscopy (AAS)

Atomic absorption spectroscopy (AAS) analysis is performed to determine the concentration of metal ions present in the aqueous solution of both samples (on the order of ppm). The result of AAS analysis as described in supplementary information in detail gives us the information about the stoichiometry of the samples. For the NP sample, Cu/ Fe ratio is found to be 0.995:2 and for NS sample, Cu/ Fe ratio is found to be 0.784:2.

Structural analysis by X-ray diffraction

Figure 1 depicts the Rietveld refined x-ray powder diffraction (XRD) patterns for NP and NS sample. All the Bragg reflections observed for both samples corresponding to single cubic $CuFe_2O_4$ phase (JCPDS File Card No. 77-0010) of space group $Fd\bar{3}m$. No additional peaks of any other phase (CuO or Fe_2O_3) are detected. The average crystallite size for NP and NS sample as determined using the well known Debye-Scherer formula, are found to be 9 nm and 14 nm, respectively. The experimental values of lattice constant (a) are determined to be 8.4031 Å and 8.3745 Å for NP and NS sample, respectively.

From the Rietveld powder refinement study, we determine the mean lattice parameter (a), oxygen positional parameter (u) and isotropic size ($<d_{iso}>$) for both samples as contained in Table 1. The refined value of lattice parameter for both samples is similar to that observed from experimentally determined value of lattice parameter. The value of lattice parameter reported by many authors for cubic $CuFe_2O_4$ system varies from 8.37 Å to 8.42 Å.[38, 39] This difference in the value of lattice parameter is due to the change in the degree of inversion or stoichiometric proportion of the cations depending on the synthesis technique of the material. In the present case, a relatively lower value of lattice parameter is observed for NS sample as compared to NP sample, which may be due to lesser concentration of Cu^{2+} ions at octahedral (B) sites[40]. In AAS study, we have observed that Cu/Fe ratio is lower for NS sample than that for NP sample. As the ionic radius of Cu^{2+} (0.72 Å) is greater than Fe^{3+} (0.64 Å), the absence of Cu^{2+} ion at some of the octahedral sites lead to lattice compression and hence, the decrease in lattice constant (a) is observed. The oxygen positional parameter (u) for both samples as obtained from the refinement differs from its ideal value (0.375) for fcc close-packed spinel lattice. The spinel structure has space group $Fd\bar{3}m$ (O_7^h) and can be described as 32 oxide ions in nearly closed packing with eight of the 64 tetrahedral sites and sixteen of the 32 octahedral sites normally occupied by

cations. Taking origin at one of the tetrahedral sites, *u* has a value equal to 0.375 for which the arrangement of O^{2-} ions equals exactly a close packing, but in actual spinel lattice, this ideal pattern is slightly disturbed. In the non-ideal spinel structure, the oxygen ions are displaced along [111] direction away from the tetrahedral position so that it forms expanded tetrahedral lattice sites without changing the overall $\bar{4}$3m symmetry. At the same time the oxygen ion connected with the octahedral site moves in such a way to shrink the size of the octahedral site assuming 3m symmetry. This deviation is quantified by altering the lattice parameter as well as the *u* parameter which is usually greater than 0.375 in this case.[38] The *u* parameter for both samples are greater than 0.375, but it is relatively higher (0.3856) for the NS sample as compared to the u parameter (0.3849) of NP sample. This is due to different synthesis conditions and different experimental precursors used to prepare the NP and NS sample.

This behavior is also reflected in the enlargement of the average tetrahedral metal-oxygen bond length (R_{OA}) and diminution of the average octahedral metal-oxygen bond length (R_{OB}) for NS sample as compared to NP sample (see Table 2). According to the typical equations,[41] as listed in the supplementary information, the interionic distance (cation-anion bond length in A site, R_{OA}, and B site, R_{OB}, tetrahedral edge, d_{AE}, shared and unshared octahedral edges, d_{BE}, d_{BEU}) for both NP and NS sample are determined using the refinement parameters (oxygen positional parameter, *u* and lattice parameter, *a*). The average tetrahedral metal-oxygen bond length (R_{OA}) for NS sample is enhanced while; the average octahedral metal-oxygen bond length (R_{OA}) of NS sample is shortened as compared to NP sample (see Table 2). This leads to believe one that the tetrahedral and octahedral symmetry of NS sample is different from that of NP sample. The cation distribution for NP sample is estimated using the refinement results as described in the supplementary information in detail and is given by

$$(Cu^{2+}_{0.08}\,Fe^{3+}_{0.92})_A\,[Cu^{2+}_{0.92}\,Fe^{3+}_{1.08}]_B.$$

The isotropic size value obtained from the refinement analysis for the NP sample is consistent with the value as obtained from the Scherrer equation. However, for the NS sample, these two values differ significantly, which apparently seems incoherent but is further substantiated in the proceeding section.

Morphology and microstructural study by FESEM and HRTEM

Field emission scanning electron microscope (FESEM) images are shown in Figure 2. It can be seen in Figure 2(a) that the NS sample contains uniformly distributed spherical assemblies with mean size ~ 90 nm. This observation can be correlated with the isotropic size value obtained previously from the Rietveld refinement analysis of the XRD data for the NS sample. A cursor inspection of the FESEM images suggest that the nanospheres are actually composed of several primary nanoparticles of size 10-14 nm. This value is in close agreement with the average crystallite size obtained from the Scherrer equation for the NS sample. On the other hand, the FESEM image of the NP sample in Figure 2(b) shows agglomerated nanoparticles with random morphology.

The microstructural analysis of both samples is further carried out by transmission electron microscopy (TEM) and the micrographs are depicted in Figure 3. TEM micrograph of the NP sample illustrates well separated nanoparticles with mean diameter of ~ 9 nm as shown in Figure 3(a). High resolution TEM image in Figure 3(b) shows an almost spherical nanoparticle ~10 nm in diameter, oriented along the [311] plane of the copper ferrite structure, confirming the crystallinity of the material.

TEM micrograph of NS sample in Figure 3(c) reveals the presence of 10-14 nm primary nanoparticles arranged in spherical aggregates with a mean size of ~ 90 nm exhibiting a sponge-like nanoporous structure. The image obtained in high resolution mode as shown in Figure 3(d) clearly shows the nanocrystalline lattice fringe with the plane oriented along the [311] direction. The electron micrographs reveal that the primary nanoparticles are almost spherical and uniformly assembled to construct the spherical nanostructure.

Infra-red and Raman spectroscopy

The unit cell of fcc copper ferrite system belongs to the $Fd\bar{3}m$ (O_h^7) space group, with eight molecules per unit cell (Z = 8), in which Fe/Cu, Fe and O atoms occupy 16d (D_{3d}), 8a (T_d) and 32e (C_{3v}) Wyckoff sites, respectively. Since each structure contains 14 atoms in the primitive unit cell, there are 42 degrees of freedom and, consequently, 42 phonons are permitted for the structures. Using the Factor Group Analysis, the zone-center vibrational modes distribution is decomposed in terms of the irreducible representations for the O_h factor group and are following

$$A_{1g} \oplus 2A_{2u} \oplus E_g \oplus 2E_u \oplus F_{1g} \oplus 5F_{1u} \oplus 3F_{2g} \oplus 2F_{2u}$$

Among these phonon modes, four of $5F_{1u}$ are IR-active in the spectral region v_1 (630-560 cm^{-1}), v_2 (525-390 cm^{-1}), v_3 (380-335 cm^{-1}) and v_4 (300-200 cm^{-1}). The v_1 band is assigned to the intrinsic stretching vibration of metal cations at the tetrahedral site, while the v_2 band is attributed to metal cations in the octahedral site.[42] The bands v_3 and v_4 generally found in far infra-red region are assigned to complex vibrations involving both octahedral and tetrahedral sites. The five phonon modes ($A_{1g} \oplus E_g \oplus 3F_{2g}$) are Raman-active and all are observed at ambient conditions.

Figure 4(a) displays the IR spectra of NP and NS sample taken in transmittance mode in the range from 400 cm^{-1} to 1200 cm^{-1}. The spectra clearly show the existence of two characteristic vibrational modes around 600 cm^{-1} (v_1) and 420 cm^{-1} (v_2) for both NP and NS sample as the common feature of all spinel ferrites. The different band position for the tetrahedral and octahedral complexes is due to the different values of Fe(Cu)–O bond length in respective sites. For the NP sample, the v_1 band is observed at 597 cm^{-1} and the v_2 band is observed at 428 cm^{-1}. But in case of NS sample the tetrahedral band v_1 is shifted to lower wavenumber value (582 cm^{-1}), while the octahedral band v_2 is shifted to higher wavenumber value (432 cm^{-1}). The lower band value for the tetrahedral site is attributed to the stretching of tetrahedral M^{2+}-O^{2-} bonds. On the other hand, the higher band value for the octahedral site is due to the shifting of octahedral M^{2+} ions towards O^{2-} ions. These results are consistent with the average tetrahedral and octahedral M^{2+}-O^{2-} bond lengths (R_{OA}, R_{OB}) as obtained from the Reitveld structure refinement results.

Figure 4(b) shows the Raman spectra of NP and NS samples taken in the range from 100 cm^{-1} to 800 cm^{-1} at room temperature. Both spectra exhibits five characteristic bands around 215, 278, 481, 586 and 656 cm^{-1}, all of those are assigned to the cubic inverse-spinel copper ferrite.[43] Additionally, an intense band around 388 cm^{-1} and a weak band at 625 cm^{-1} observed for both samples and some of the Raman bands are very broad, suggesting that those are may be composed of more than one Raman band. Therefore, the number of observed Raman phonon mode is not consistent with cubic symmetry. For the cubic ferrite structure, the bands around 215, 278, 481, 586 and 656 cm^{-1} are assigned to F_{2g} (1), E_g, F_{2g} (2), F_{2g} (3) and A_{1g}, respectively. To explain the appearance of the extra Raman peaks, we propose a breakdown of the momentum conservation rule, since the wavelength of the exciting radiation (532 nm) is much larger than the

particle diameter (~10 nm). In the case of a perfect crystal with size much larger than the wavelength, *i.e.*, k = 0, it means that only the phonons near the center of Brillouin zone are allowed in the Raman scattering due to the momentum conservation rule. However, for nanoparticles, the momentum conservation rule is violated and phonons for k ≠ 0 become allowed in the Raman scattering. Therefore, we believe that for k ≠ 0, the inversion center of the cubic centrosymmetric crystal is absent, which explains the appearance of extra Raman modes in the spectra. Additionally, a systematic shift of the vibrational frequency of the Raman modes and considerable change in relative intensity is also observed in the spectra of NP and NS samples. The Raman frequency depends on the Fe(Cu)–O bond distance, which modifies with both the alteration of the lattice parameter and ionic radii of divalent ions. This shift of the vibrational frequency is attributed to the different value of Fe(Cu)–O bond length for NP and NS sample and this supports the Rietveld refinement analysis and IR spectroscopy results.

Mössbauer spectroscopy

Zero-field Fe^{57} Mössbauer spectra of NP and NS sample is recorded at room temperature as shown in Figure 5. The spectra are fitted as the probability distribution of the hyperfine field using the program package NORMOS[37] and the fitting parameters for both samples are listed in Table 3. The spectrum of ~9 nm $CuFe_2O_4$ nano particles (NP) exhibit a strong quadrupole doublet at the centre of the spectrum superimposed on a magnetically split sextet spread across the spectrum indicating the presence of a finite size distribution in the sample. The existence of the strong doublet signifies that large fraction (33%) of particles are superparamagnetic at room temperature in the time of measurement. When the dimension of a magnetic particle is below a certain critical limit, the magnetic anisotropy energy (K_EV) of the particle is smaller than the average thermal energy (k_BT). Due to very small relaxation time (τ), the magnetic moment flips

rapidly so that the effective moment during the time of measurement becomes zero ($K_EV << k_BT$). This causes the collapse of a multiplet to a superparamagnetic doublet.

The value of isomer shift (δ) for the NP sample is characteristic of Fe^{3+} charge state (δ ~ 0.5 mm/s) implying that Fe ions present in both A and B site in trivalent state only.[44] The Mössbauer spectra of NS sample exhibit two sextets corresponding to the iron ion at two different sites, *i.e.*, tetrahedral (A) and octahedral (B) site. Additionally, a weak doublet with small area ratio is also found which is due to the presence of some nanoparticles lying below the critical size limit for superparamagnetic relaxation at the measurement time scale. The isomer shift (δ) values corresponding to tetrahedral (δ_A) and octahedral (δ_B) sites of NS sample as listed in Table 3 indicates that Fe^{3+} ions are in high spin state (δ ~ 0.5 mm/s).[44] The δ_A and δ_B values for NS sample found to be 0.43 and 0.30 mm/s, respectively. The different value of isomer shift for NP and NS sample illustrates that the s-electron density at the Mössbauer active nuclear site is significantly affected by the preparation technique of the samples. The different value of the average Fe^{3+}-O^{2-} bond length at respective site for the two samples as determined from the Rietveld refinement analysis supports this observation. The ferric character of the Fe ion is also manifested by the magnitudes of the magnetic hyperfine fields. Since ferric ions have neither orbital nor dipolar contributions[45] to the magnetic hyperfine field, the magnetic hyperfine field is proportional to the spin of the ferric ion. The quadrupole shift of NS sample for the A pattern is much smaller in magnitude than that of the B pattern. This suggests that the two sextets originate from A (tetrahedral) and B (octahedral) sites, respectively, as the local symmetry of the A-site is close to cubic T_d while that of the B-site is close to trigonal D_{3d}.

The average hyperfine field (B_{hf}) for the NS sample is higher than that of the NP sample as listed in Table 3. This is due to higher net magnetic moment per unit formula for NS sample as

determined by the concentration of Fe^{3+} ion at octahedral site. The relative area ratio of two Fe^{3+} sextets for NS sample reveals that the concentration of Fe^{3+} ions at octahedral (B) site is higher than that at the tetrahedral (A) site. However, the AAS analysis confirmed that the Cu/Fe ratio is 0.784:2 for NS sample, which clearly indicates the formation of non-stoichiometric copper ferrite with some Cu-deficient lattice sites. Therefore, the lattice structure should have some point defects. In Fe-rich composition, the cation vacancies are most probably formed at the octahedral (B) lattice sites, as in the case of maghemite, $(Fe^{3+})_A[Fe^{3+}_{5/3}\square_{1/3}]_BO_4$.[40] Therefore, the non-stoichiometric cation distribution for the NS sample can be represented as

$$(Cu^{2+}_{x}Fe^{3+}_{1-x})_A\,[Cu^{2+}_{(1-x-y)}Fe^{3+}_{(1+x)}\square_{y}\,]_B$$

where, $\square$ represents the cation vacancy at the B-site and y represents the correction factor for stoichiometric proportion in the sample. The value of x can be extracted from the Mossbauer data using the following equation:

$$\frac{S_A}{S_B} = \frac{1-x}{1+x} \qquad (2)$$

where, $\frac{S_A}{S_B}$ is the relative area ratio of the A sites to the B sites. From the AAS analysis, the value of y is found to be 0.22, which is further used to estimate the actual cation distribution of NS sample and is given by

$$(Cu^{2+}_{0.176}Fe^{3+}_{0.824})_A[Cu^{2+}_{0.604}Fe^{3+}_{1.176}\,\square_{0.22}]_B$$

This clearly suggests that the concentration of Fe^{3+} ions at octahedral site and consequently, the net magnetons per unit formula for NS sample is higher than that of NP sample. Accordingly, the

value of average hyperfine field for the NS sample is higher as compared to NP sample. The magnetic study of the samples also reveals higher saturation magnetization (M_S) for NS sample and is discussed in the proceeding section.

Magnetic property study

The field-cooled (FC) and zero field-cooled (ZFC) magnetization is recorded in the temperature range from 5 K to 300 K in presence of an external field of 100 Oe for both NP and NS samples as shown in Figure 6. The ZFC curve of the NP sample exhibit a broad maximum at a temperature (T_{max} ~ 25 K), which for non-interacting particles, is directly proportional to the mean blocking temperature (T_B). However, if a distribution of sizes is present, this peak temperature can deviate from the true blocking temperature (T_B).[46] In ZFC mode when temperature increases from 5 K, some of the nanoparticles with smaller size overcome the anisotropy energy barrier and start to align themselves along the direction of applied field; consequently the net magnetization increases. Further increase in temperature above T_{max} leads to random thermal fluctuation of the superspins as the relaxation time get reduced below the measurement time scale ($\tau < \tau_o$) and the overall magnetization reduces. The broad nature of peak as observed in ZFC curve is attributed to the fact that in the real case of an ensemble of magnetic nanoparticles with easy axis randomly oriented in the entire space and with the presence of a finite size distribution, the effective anisotropy energy barrier is distributed over a certain range. In the FC mode, the magnetization continuously increases as temperature decreases from 300 K to 5 K. In case of the NS sample, $M_{FC}(T)$ is flattened bellow a particular temperature (T_G at 18 K) exhibiting temperature independent behavior while, it decreases gradually as the temperature increases above ~ 18 K. This is indicative of typical co-operative freezing (spin-glasslike) behavior of the strongly interacting particles in magnetically frustrated system.[47] The

irreversibility of $M_{FC}(T)$ and $M_{ZFC}(T)$ is one of the characteristic features of a spin glass system.[48,49] Figure 5 clearly showing that $M_{FC}(T)$ and $M_{ZFC}(T)$ curves of NS sample diverge in the whole temperature range and the divergence increases with decreasing temperature. In case of NP sample, $M_{FC}(T)$ and $M_{ZFC}(T)$ coincides at 250 K, which is the irreversible temperature (T_{irr}) related to the blocking of the biggest particle. The ZFC curve of the NS sample exhibit a maximum at a temperature (T_{max} ~ 24 K) which is almost the same as for the NP sample indicating that the arrangement of nanoparticles in spherical aggregates does not stimulate relevant modification in the supermagnetic behavior. Nevertheless, the ZFC peak for the NP sample is slightly narrower as compared to the NS sample, which indicates the narrower distribution of anisotropy energy in NP sample as compared to NS sample or a relatively strong interparticle interaction in NS sample.[50]

The field dependence of magnetization for NP and NS sample is investigated at various temperatures between 5 K and 300 K. The saturation magnetization (M_S), reduced remanent magnetization (M_R/M_S), and coercive field (H_C) as extracted from hysteresis loops are given in Table 4. A comparison between the typical $M(H)$ loops of NP and NS samples measured at 5 K and 300 K are shown in Figure 7. Figure 7(a) illustrates that both NP and NS samples exhibit clear hysteresis loops with coercivity of 956 Oe and 456 Oe respectively at low temperature (5 K). In addition, it is shown that the magnetization at 5 K is clearly larger than that of 300 K. This is due to the fact that at 5 K, the thermal fluctuation is much lesser than that at 300 K and consequently, the magnetic moments can be aligned more orderly due to exchange interaction, and the projection of the moments in the direction of the applied field is larger. The low-temperature hysteresis behavior of both samples can be correlated with strong ferrimagnetic interaction between the sublattices in the spinel structure owing to very low thermal fluctuation

of magnetic moments. Even at room temperature (300 K), both NP and NS samples show non-vanishing coercivity. The strong sextet in the room temperature Mössbauer spectra of the NP sample suggests that a large fraction (67%) of particles are ordered magnetic even at 300 K and these particles may contribute to the room temperature coercivity. However, the nature of the hysteresis loop of NP and NS samples differ significantly. For NS sample, a step-like rectangular hysteresis loop is observed at both temperatures while, a smooth S-shaped unsaturated hysteresis loop is obtained for NP sample (Figure 7). The non-saturation of hysteresis loop observed at 5 K for NP sample may be due to the glass-like freezing of surface spins at low temperature[51], while at 300 K, the high field quasilinear nature of $M(H)$ curve indicates superparamagnetic behavior. This strongly suggests the uniaxial nature of magnetic anisotropy in NP sample, whereas the step like hysteresis loop suggests cubic anisotropy in NS sample.[52]

In some recent literature, it has been found that for an ensemble of magnetic nanoparticles there is a typical single domain size range where particles do not show superparamagnetic behavior in external field but exhibit non-vanishing hysteresis loop.[53, 54] However, there is no such report showing step-like hysteresis behavior of $CuFe_2O_4$ nanoparticles as per our knowledge. This motivates us to study the temperature dependence of magnetization reversal of $CuFe_2O_4$ nanoparticles assembly in detail. The step-like magnetization reversal is observed at each measuring temperature between 5 K and 300 K for the NS sample. This result leads to believe one that the step-like rectangular hysteresis loop is somehow associated with the formation of spherical ensemble of nanoparticles.

The saturation magnetization (M_S) versus temperature plot for NP and NS sample is shown in Figure 8. A decrease in saturation magnetization from its bulk value[17, 55] is observed for both NP and NS samples. This is due to a low degree of crystallinity associated with the low synthesis

temperature used in the preparation methods. For NS sample, M_S exhibits gradual increase as the temperature decreases, and the change of M_S becomes smaller and smaller with a flat M_S (~7.53 emu/g) bellow 200 K. But for NP sample, M_S decreases rather sharply with increasing temperature. Since the saturation magnetization is mainly determined by magnetons and their orientation in the system and not susceptible to the change of microstructure, it is more feasible that M_S will show the same variation with temperature for both samples. In the case of ordered magnetic systems, the thermal behavior of the magnetization is related to the presence of low energy collective excitations (spin waves or magnons) and it shows a decrease in the spontaneous magnetization with increasing temperature.[51] Such a model well works for infinite systems if the gap, induced in the dispersion relation of spin waves, is zero.[56] But the temperature dependence of magnetization for nanoparticles differ from that of bulk materials since the spatial confinement reduces the number of degrees of freedom generating an energy gap in the corresponding spin-wave spectrum. However, the rapid decrease of M_S with increasing temperature observed in NP sample is mainly due to the interplay of thermal energy and applied field. Basically, the applied field offers the energy to make the moments ordering, while the thermal energy destroys such order. With the decrease in temperature, the effect of thermal energy becomes weaker, thus making it easier for the magnetic moments to flip to the direction of the applied field. In room temperature Mössbauer study, we have observed that a large fraction of particles (33%) are superparamagnetic at room temperature as determined by the presence of a strong doublet in the spectra of NP sample, therefore the contribution of these fine particles to M_S is getting lesser and lesser with increasing temperature. It is observed that the value of saturation magnetization (M_S) of NS sample is much higher as compared to NP sample in the whole temperature range except at 5 K. Theoretically, a higher value of M_S is expected as

the concentration of Fe^{3+} ions at octahedral site in the NS sample is higher than the NP sample and the magnetons of Fe^{3+} ($5\mu_B$) is higher as compared to that of Cu^{2+} ($1\ \mu_B$). This leads to an increase in net magnetons per unit formula for NS sample. The room temperature Mössbauer study is consistent with this result revealing higher average hyperfine field (B_{hf}) for NS sample as compared to NP sample.

The most interesting temperature dependence is observed in case of reduced remanent magnetization (M_R/M_S) and coercivity (H_C) for NS sample as displayed in Figure 9. The reduced remanent magnetization (M_R/M_S) for NP sample varies from 0.5 at 5 K to 0.2 at 300 K, while for NS sample, the ratio $M_R/M_S \sim 1$ in the temperature range from 5 K to 100 K and then decreases to 0.7 at 300 K. This suggests the typical uniaxial anisotropy in NP sample and the cubic anisotropy in NS sample.[57] Due to the presence of Cu^{2+} (d^9) ions with nonzero orbital moment, bulk $CuFe_2O_4$ is described by cubic anisotropy of magnetocrystalline origin.[58] But at the nanoscale, both the cubic and uniaxial anisotropy may coexist with completely uniaxial anisotropy for particles with much lower size.[59-61] In general, the magnetization reversal of particles with cubic anisotropy is dissimilar from those of an ensemble of particles with uniaxial anisotropy. Due to the presence of six easy directions in the system with cubic anisotropy, the probability that randomly oriented particles have an easy direction close to the direction of the applied field is very high. Therefore, a much higher value ($M_R/M_S \sim 0.83$) of remanence magnetization of the system with cubic anisotropy is expected.[62-65] In the present case, the reduced remanent magnetization is ~ 0.5 in the NP sample at low temperature (5 K), which is consistent with uniaxial anisotropy.[66] On the other hand, the NS sample exhibits $M_R/M_S = 1$, which is typical for magnetic system with cubic anisotropy.[67]

The coercive field (H_C) is a very important parameter in particulate media for application in magneto-recording. The temperature dependence of coercivity (H_C) of NP and NS sample is shown in Figure 9(a). For NP sample, coercivity (H_C) decreases monotonously with increasing temperature following the typical superparamagnetic nature of uniaxial single domain particles.[68, 69] For single-domain non-interacting nanoparticles the temperature dependence of H_C can be described by Kneller's law which is given by[70]

$$H_C = H_{C_0}\left[1 - \left(\frac{T}{T_B}\right)^{\frac{1}{2}}\right] \qquad (3)$$

where H_{C_0} is the coercivity at 0 K and T_B is the superparamagnetic blocking temperature. As shown in the inset of Figure 9(a), the data of H_C between 5 K and 300 K for NP sample is well fitted to equation (3) indicating that H_C varies linearly with $T^{1/2}$ for NP sample, and the T_B is fitted to be 335 K. Therefore, if neglecting the interparticle interactions, it is expected that when the temperature is above 335 K, the intrinsic anisotropy barrier will be overcame by the thermal energy, and the H_C will become zero. On the other hand, a huge anomaly in temperature dependence of coercivity (H_C) is observed in case of NS sample. H_C slightly increases with reducing temperature, reaching a maximum value of 558.2 Oe at 280 K. However, a sharp decrease in H_C is observed between 200 and 100 K, with H_C = 104.4 Oe at 50 K. When temperature is further reduced H_C sharply increases again, achieving a value of 456.2 Oe at 5 K. To clarify this unusual temperature dependence of coercivity for NS sample, the effective anisotropy constant (K_E) at different temperature is determined. It is well known that coercivity is a direct consequence of K_E/M_s ratio for single domain non-interacting particles.[71] Depending on the nature of anisotropy of the system, K_E/M_s ratio is multiplied by a constant term γ (for nanoparticles with cubic anisotropy, γ = 0.64 and for nanoparticles with uniaxial anisotropy, γ =

0.5). To determine the effective magnetic anisotropy (K_E) at different temperatures we fitted the high field part of $M(H)$ data to 'law of approach' (LA) to saturation. For a polycrystalline magnetic material, the 'law of approach' (LA) to saturation equation can be described as[66]

$$M(H) = M_S\left(1 - \frac{a}{H} - \frac{b}{H^2} - \cdots\right) + \chi_p H \qquad (4)$$

where $M(H)$ is the magnetization in a field H, M_S is the saturation magnetization. The term χ_p is the forced magnetization coefficient that describes the linear increase in spontaneous magnetization at high fields. The inclusion of the term a/H is attributed to the strain field around dislocation in the material. The origin of the term b/H^2 is the magnetic anisotropy and the coefficient b is related to the effective magnetic anisotropy (K_E) by[66]

$$b = \frac{4K_E^2}{15M_S^2} = \frac{4\left(K_{\mathrm{sh}}^2 + K_{\mathrm{st}}^2 + K_{\mathrm{sf}}^2 + \frac{2}{7}K_1^2\right)}{15M_S^2} \qquad (5)$$

where, K_{sh}, K_{st}, K_{sf} and K_1 are the shape anisotropy, stress anisotropy, surface anisotropy and magnetocrystalline anisotropy respectively.

Table 5 contains all the fitting parameters along with the R^2 value, which suggests the quality of fitting is excellent for each set of high field $M(H)$ data. The value of M_S as obtained from the best fitted result is plotted against temperature and is shown in Figure 10(a). The parameters, M_S and b, as obtained through the fitting are used to determine the effective magnetic anisotropy (K_E) using equation (5) at different temperatures. For instance, the effective anisotropy calculated at 300 K, $K_E = (0.34 \pm 0.02) \times 10^5$ erg/cm^3, is similar to that of 11 nm cubic $CuFe_2O_4$ nanoparticles[72]. Figure 10(a) presents the variation of effective anisotropy constant (K_E) with temperature, more or less the same anomalous nature of temperature dependence of K_E is

observed as of H_C in the temperature range from 5 K to 200 K. But above 200 K, the temperature dependence of H_C and K_E differ noticeably. This suggests that K_E plays a governing role to determine H_C below 200 K, since M_S is found to be constant bellow 200 K. Whereas, in the high temperature region, both K_E and M_S decreases with increasing temperature keeping K_E/M_S ratio almost constant. Considering cubic anisotropy ($\gamma = 0.64$), experimental H_C and estimated value of $\gamma K_E/M_S$ (theoretical H_C) are plotted against temperature as depicted in Figure 10(b). The temperature dependence of coercivity (H_C) shows analogous behavior as that of $\gamma K_E/M_S$ ratio. It is well known that coercivity (H_C) of a multi-domain particle increases as the size decreases and at a critical size limit (R_{SD}) the particle is converted into single domain state. The critical single domain size limit (R_{SD}) for spherical nanoparticle depends on $K_E^{1/2}/M_S^2$.[73] Therefore, at high temperature range (above 200 K), where effective anisotropy (K_E) is large and M_S is low, the particle size of the NS sample, $d_{NS} < R_{SD}$ and the particles are single domain. However, as temperature is lowered and K_E decreases, the critical condition where $d_{NS} \sim R_{SD}$ is reached and, upon further R_{SD} reduction by lowering the temperature upto 50 K, the particles lose their single-domain character. This fact reveals the diminution of coercivity to 104 Oe at 50 K. The further increase in H_C observed at lower temperatures can be ascribed to an increase in effective anisotropy (K_E), which is probably related to the predominance of surface anisotropy at low temperature due to glass-like freezing of surface spins.[74]

The room temperature coercivity of NS sample is much larger than that of the NP sample indicating the higher value of K_E at 300 K as compared to the NP sample. As the primary nanoparticles of the spherical assembly are almost spherical, shape anisotropy is not likely to play a significant role in the large room-temperature coercivity. The surface anisotropy contribution is also negligible at high temperature. This leads to believe one that the large room

temperature coercivity of the NS sample is mainly due to the contribution of magnetocrystalline anisotropy, which is determined by the strength of the spin-orbit coupling. For NS sample, the strong spin-orbit coupling can be ascribed to the significant modification of some of the Fe^{3+}/Cu^{2+}- O^{2-} bond distances. We have observed that the degree of deformation of the tetrahedral/octahedral polyhedra for NS sample is high as compared to the NP sample. The average tetrahedral metal-oxygen bond length (R_{OA}) is higher and the average octahedral metal-oxygen bond length (R_{OB}) is lower for NS sample as compared to NP sample (see Table 2). Although, transition metal oxides are characterized by weak spin-orbit coupling due to the so called orbital quenching in weak ligand field[75], a nonzero value of orbital moment is possible due to the presence of some distorted polyhedra. In general, a nonzero value of orbital moment is not expected with a half-filled $3d^5$ electronic state of Fe^{3+} ions, but the distortions of Fe^{3+} coordination polyhedra may result in Fe 3d-O 2p mixing and O 2p to Fe 3d charge transfer which, together with ligand-field effect, lifts the electronic degeneracy leading to a nonzero orbital moment.[76, 77] Consequently, the spin-orbit coupling strengthens and leads to a large room temperature coercivity for NS sample.

Similarly, the reduction in H_C at low temperatures (50 K), and the related decrease in the anisotropy constant (K_E) at 50 K, can be due to the weakening of spin-orbit interactions. The origin of the low temperature collapse of magnetic anisotropy can be associated with the temperature dependent modification of Cu/Fe-O bond distances. Orbital moment instability has been previously accounted in $Nd_2Fe_{14}B$ at the spin reorientation transition temperature[78] and coinciding with a lattice distortion. Noticeably, the decrease in K_E and the collapse of H_C in the present case only take place in a limited temperature range (50-200 K). As discussed by García et al.[78] for $Nd_2Fe_{14}B$, this suggests that these effects are not wholly related to the different low

and high temperature magnetic phases but to the phase transition itself and the instantaneous change in order parameter *e.g.*, Cu/Fe-O bond length in the present case. Detailed study regarding the temperature dependent modification of bond lengths and related orbital moment instability are in progress.

Although, the nature of the $\gamma K_E/M_S$ versus temperature plot is similar to the temperature dependence of coercivity (H_C) curve, the exact experimental values of coercivity are slightly different. This inconsistency should be discussed from a different point of view. Both the reduced remanent magnetization (M_R/M_S) and coercivity for the NS sample are distinct from those of the NP sample and H_C cannot be fairly reproduced by K_E/M_S values. This directs one to believe that the different magnetic properties observed in the NS sample are related to the arrangements of nanoparticles in spherical aggregates.

The increase of reduced remanent magnetization (M_R/M_S) for NS sample can be due to either preferential orientation of the magnetic easy axes, as already observed with maghemite nanocrystals[3], or to the formation of ferromagnetic domains induced by dipolar interactions. According to Ngo and Pileni, the increase of M_R/M_S and the step-like rectangular hysteresis loop is due to a progressive partial orientation of the easy magnetization axes along the applied field.[3] A preferential orientation of the magnetic easy axes along the applied field direction depends on the ratio of the anisotropy energy upon thermal energy, K_EV/k_BT. At much lower temperature, when the anisotropy energy K_EV is much greater than the thermal energy, the nanoparticles can rotate on themselves under an applied field with their magnetic moments lying along one of the magnetic easy directions. A preferential orientation of the easy magnetic axes is then expected. By considering the FC magnetization values of NP and NS samples at temperature much below the mean blocking temperature it is possible to verify the degree of alignment of the easy

magnetic axes of the nanoparticles in both samples. A calculation is carried out within the assumption, involving trial moves of the orientation of the moment direction and easy axis of an ensemble of nanoparticles. Specifically, as detailed described in supplementary information, the ratio between the FC magnetization of a partially aligned system ($M_{\mathrm{FC}}^{\mathrm{align}}$) and the FC magnetization of randomly oriented system (M_{FC}) can be written as

$$M_{\mathrm{FC}}^{\mathrm{align}}/M_{\mathrm{FC}} = 1 + \alpha(3\cos^2\beta - 1) \qquad (6)$$

where β is the average angle between the easy magnetic axis and applied magnetic field, α is the fraction of nanoparticles having aligned easy axes. If all the particles are randomly oriented, α = 0 and $M_{\mathrm{FC}}^{\mathrm{align}}/ M_{\mathrm{FC}} = 1$, while the presence of a fraction of particles with oriented easy axes leads to $M_{\mathrm{FC}}^{\mathrm{align}}/ M_{\mathrm{FC}} \neq 1$. The FC magnetization value recorded at 10 K under an applied field of 100 Oe is different for the NP and NS samples, giving $M_{\mathrm{FC}}^{\mathrm{NS}}/M_{\mathrm{FC}}^{\mathrm{NP}} = 2.4$.

This confirms high degree of alignment of the magnetic easy axes along the applied field in the NS sample. Actualy, it is logical that the iso-oriented structure present in each spherical assembly leads to an modification of the random situation present in the NP sample (see Figure 11). Therefore, the increase in M_R/M_S can be assignd to the preferential orientation of the anisotropy easy axis. Considering that all the magnetic easy axes are aligned, the hysteresis loop measured when the field is parallel to the easy axes is expected to be rectangular ($M_R/M_S = 1$)[79], whereas, along a perpendicular direction (hard direction), it is a smoother loop with no coercive field ($M_R/M_S = 0$). Then, for an assembly of nanoparticles with a random distribution of easy axes, the value of M_R/M_S should be ~0.5.[80] Therefore, the enhanced reduced remanence magnetization (M_R/M_S) and the step-like rectangular hysteresis loops observed in NS sample can

be explained on account of a high degree of orientation of magnetic easy axis along the applied field in the spherical assembly of nanoparticles compared to the randomly oriented nanoparticles.

Conclusions

The influence of $CuFe_2O_4$ nanoparticles "arrangement" on magnetic anisotropy and the degree of alighnment of magnetic easy axis has been investigated. Although, the magnetic property of nanoscale materials are mainly influenced by particle dimension, the instability in magnetic anisotropy and the orientation of magnetic easy axis plays a profound role in physics and chemistry of these materials. The symmetry of crystal structure and chemical composition of materials, which are decided by synthesis conditions, vastly affects the magnetic anisotropy of materials. The randomly oriented nanoparticles (NP) demonstrate typical features of uniaxial anisotropy ($M_R/M_S \sim 0.5$), while the spherical asemblies of nanoparticles (NS) exhibit step-like hysteresis loops ($M_R/M_S \sim 1$) suggesting cubic anisotropy. The higher coercive field of NS sample as compared to NP sample is due to the lattice distortion assisted nonzero orbital moment leading to high magnetocrystalline anisotropy in the system. These findings may be of interest and importance for establishing a clear physical picture of nanoscale ferrite materials and may be useful to improve the performance of related multifunctional devices. The formation of iso-oriented spherical assembly leads to a high degree of orientation of easy axis, stimulating an increase in reduced remanent magnetization ($M_R/M_S \sim 0.5 \rightarrow M_R/M_S \sim 1$) of the material. In this work, the magnetic property (M_R/M_S, T_B, Hc) of $CuFe_2O_4$ nanoparticles have been directly associated with the synthesis conditions and nanoparticles "arrangement". The elementary nature of this study can open interesting potentials for particular applications (hyperthermia, magnetic recording, etc.), permiting one to control the thermal stability (M_R/M_S), magnetic anisotropy (Hc), and superparamagnetic features of nanomaterials with a certain particle size.

Acknowledgement

The authors like to thank the University Grants Commission (UGC), the Govt. of India for University with potential for excellence scheme (UPE-II). We also wish to thank the Department of Science and Technology (DST), the Government of India and TEQIP programme for financial support.

Reference

[1] M. P. Proenca, C. T. Sousa, A. M. Pereira, P. B. Tavares, J. Ventura, M. Vazquez and J. P. Araujo, *Phys. Chem. Chem. Phys.*, 2011, **13**, 9561

[2] M. Vasilakaki and K. N. Trohidou, *J. Phys. D: Appl. Phys.*, 2008, **41**, 134006

[3] A. T. Ngo and M. P. Pileni, *J. Phys. Chem. B*., 2001, **105**, 53

[4] M. El-Hi1o, K. O'Grady and R. W. Chantrell, *J. Magn. Magn. Mater.*, 1992, **114**, 307

[5] W. F. Jr. Brown, *Phys. Rev.*, 1963, **130**, 1677

[6] L. Néel, *Ann. Geophys.*, 1949, **5**, 99

[7] T. D. Schladt, K. Schneider, H. Schild and W. Tremel, *Dalton Trans*., 2011, **40**, 6315

[8] S. Mørup, M. F. Hansen, C. Frandsen, *Beilstein J. Nanotechnol.*, 2010, **1**,182

[9] K. J. Kim, J. H. Lee, S. H. Lee, *J. Magn. Magn. Mater.*, 2004, **279**, 173

[10] C. Covaliu, J. Neamtu, G. Georgescu, T. Malaeru, C. Cristea, I. Jitaru, *Dig. J. Nanomater. Bios.*, 2011, **6**, 245

[11] S. Chikazumi, in *Physics of Ferromagnetism*, ed. J. Birman, S. F. Edwards, R. Friend, C. H. L. Smith, M. Rees, D. Sherrington, G. Venezians, Oxford University Press, Oxford, 2nd edn., 1997, pp. 201

[12] C. R. Alves, R. Aquino, M. H. Sousa, H. R. Rechenberg, G. F. Goya, F. A. Tourinho, J. Depeyrot, *J. Metastable Nanocryst. Mater.*, 2004, **20**, 694

[13] Z. Peng, J. Y. Hwang, M. Andriese, *IEEE Trans. Magn.*, 2013, **49**, 1163

[14] U. Jeong, X. Teng, Y. Wang, H. Yang, Y. Xia, *Adv. Mater.*, 2007, **19**, 33

[15] M. M. Rashad, R. M. Mohamed, M. A. Ibrahim, L. F. M. Ismail, E. A. Abdel-Aal, *Adv. Powder Technol.*, 2012, **23**, 315

[16] D. Prabhu, A. Narayanasamy, K. Shinoda, B. Jeyadeven, J. M. Greneche, K. Chattopadhyay, *J. Appl. Phys.*, 2011, **109**, 013532

[17] S. Roy and J. Ghose, *J. Appl. Phys.*, 2000, **87**, 6226

[18] H. Ohnishi and T. Teranishi, *J. Phys. Soc. Jpn.*, 1961, **16**, 35

[19] J. Z. Jiang, G. F. Goya, H. R. Rechenberg, *J. Phys.: Condens. Matter*, 1999, **11**, 4063

[20] I. Nedkov, R. E. Vandenberghe, T. Marinova, P. Thailhades, T. Merodiiska, I. Avramova, *Appl. Surf. Sci.*, 2006, **253**, 2589

[21] H. Hamdeh, J. C. Ho, S. A. Oliver, R. J. Willey, G. Oliveri, G. Busca, *J. Appl. Phys.*, 1997, **81**, 1851

[22] E. E. Carpenter and C. J. O'Connor, *J. Appl. Phys.*, 1999, **85**, 5175

[23] N. Moumen and M. P. Pileni, *Chem. Mater.*, 1996, **8**, 1128

[24] C. Nordhei, A. L. Ramstad, D. G. Nicholson, *Phys. Chem. Chem. Phys.*, 2008, **10**, 1053

[25] A. Banerjee, S. Bid, H. Dutta, S. Chaudhuri, D. Das, S. K. Pradhan, *Mater. Res.*, 2012, **15**, 1022

[26] S. Sun and H. Zeng, *J. Am. Chem. Soc.*, 2002, **124**, 8204

[27] V. M. Khot, A. B. Salunkhe, N. D. Thorat, R. S. Ningthoujam and S. H. Pawar, *Dalton Trans*., 2013, **42**, 1249

[28] S. Xuan, F. Wang, Y. J. Wang, J. C. Yu and K. C. Leung, *J. Mater. Chem.*, 2010, **20**, 5086

[29] B. Y. Yu and S. Kwak, *Dalton Trans*., 2011, **40**, 9989

[30] Y. Li, C. W. Park, *Langmuir*, 1999, **15**, 952

[31] R. E. Riman, in *High Performance Ceramics: Surface Chemistry in Processing Technology*, ed. R. Pugh and L. Bergström, Marcel-Dekker, U.S.A. 1993, pp. 29

[32] H. M. Rietveld, *Acta Crystallogr.*, 1967, **22**, 151

[33] H. M. Rietveld, *J. Appl. Crystallogr.*, 1969, **2**, 65

[34] R. A. Young and D. B. Willes, *J. Appl. Crystallogr.*, 1982, **15**, 430

[35] L. Lutterotti, P. Scardi, *J. Appl. Crystallogr.*, 1990, **23**, 246

[36] L. Lutterotti, *MAUD version 2.33*, 2011, Available from: http://www.ing.unitn.it/~maud

[37] R. A. Brand, *Nucl. Instrum. Methods Phys. Res. B*, 1987, **28**, 398

[38] A. T. Raghavender, S. E. Shirsath, D. Pajic, K. Zadroand, T. Milekovic, K. M. Jadhav, K. V. Kumar, *J. Korean Phys. Soc.*, 2012, **61**, 568

[39] M. U. Rana, M. Islam, T. Abbas, *Mater. Chem. Phys.*, 2000, **65**, 345

[40] D. Makovec, M. Drofenik, *J. Nanopart. Res.*, 2008, **10**, 131

[41] R. Valenzuela, in *Magnetic Ceramics*, ed. B. Dunn, J. W. Goodby, A. R. West, Cambridge University Press, Cambridge, 1994, pp. 5

[42] C. M. Julien, F. Gendron, A. Amdouni, M. Massot, *Mater. Sci. Eng. B*, 2006, **130**, 41

[43] M. Balaji, P. Chithra Lekha, D. P. Padiyan, *Vib. Spectrosc.*, 2012, **62**, 92

[44] Z. He, W. Zhang, W. Cheng, A. Okazawa and N. Kojima, *Dalton Trans*., 2013, **42**, 5860

[45] F. K. Lotgering, R. P. Van Stapele, G. H. A. M. Van Der Steen, J. S. Van Wieringen, *J. Phys. Chem. Solids.*, 1969, **30**, 799

[46] D. E. Madsen, M. F. Hansen, S. Mørup, *J. Phys.: Condens. Matter.*, 2008, **20**, 345209

[47] D. Peddis, C. Cannas, A. Musinu, G. Piccaluga, *J. Phys. Chem. C*, 2008, **112**, 5141

[48] K. Binder and A. P. Young, *Rev. Mod. Phys.*, 1986, **58**, 801

[49] P. A. Joy, P. S. Anil Kumar, S. K. Date, *J. Phys.: Condens. Matter*, 1998, **10**, 11049

[50] C. Cannas, A. Musinu, D. Peddis, and G. Piccaluga, *Chem. Mater.*, 2006, **18**, 3835

[51] R. H. Kodama, *J. Magn. Magn. Mater.*, 1999, **200**, 359

[52] S. Chikazumi, in *Physics of Ferromagnetism*, ed. J. Birman, S. F. Edwards, R. Friend, C. H. L. Smith, M. Rees, D. Sherrington, G. Venezians, Oxford University Press, Oxford, 2nd edn., 1997, pp. 514

[53] C. Caizer and M. Stefanescu, *J. Phys. D: Appl. Phys.*, 2002, **35**, 3035

[54] C. Caizer and M. Stefanescu, *Physica B*, 2003, **327**, 129

[55] G. F. Goya, H. R. Rechenberg, J. Z. Jiang, *J. Appl. Phys.*, 1998, **84**, 1101

[56] P. V. Hendriksen, S. Linderoth, and P.-A. Lingård, *J. Magn. Magn. Mater.*, 1992, **104**, 1577

[57] S. Chikazumi, in *Physics of Ferromagnetism*, ed. J. Birman, S. F. Edwards, R. Friend, C. H. L. Smith, M. Rees, D. Sherrington, G. Venezians, Oxford University Press, Oxford, 2nd edn., 1997, pp. 514

[58] J. Smit and H. P. J. Wijn, in *Ferrites*, ed. G. E. Luton, Philips Technical Library, The Netherlands, 1959, pp. 162

[59] D. Peddis, F. Orrù, A. Ardu, C. Cannas, A. Musinu, G. Piccaluga, *Chem. Mater.*, 2012, **24**, 1062

[60] R. Yanes and O. Chubykalo-Fesenko, H. Kachkachi, D. A. Garanin, R. Evans and R. W. Chantrell, *Phys. Rev. B*, 2007, **76**, 064416

[61] J. Geshev, M. Mikhov, and J. E. Schmidt, *J. Appl. Phys.*, 1999, **85**, 7321

[62] N. A. Usov, S. E. Peschany, *J. Magn. Magn. Mater.*, 1997, **174**, 247

[63] J. Garcia-Otero, M. Porto, J. Rivas, A. Bunde, *J. Appl. Phys.*, 1999, **85**, 2287

[64] J. Geshev, M. Mikhov, *J. Magn. Magn. Mater.*, 1992, **104**, 1569

[65] A. Virden, S. Wells, K. O'Grady, *J. Magn. Magn. Mater.*, 2007, **316**, e768

[66] D. L. Hou, X. F. Nie, H. L. Luo, *J. Magn. Magn. Mater.*, 1998, **188**, 169

[67] S. Chikazumi, in *Physics of Ferromagnetism*, ed. J. Birman, S. F. Edwards, R. Friend, C. H. L. Smith, M. Rees, D. Sherrington, G. Venezians, Oxford University Press, Oxford, 2nd edn., 1997, pp. 514

[68] K. Maaz, A. Mumtaz, S. K. Hasanain, M. F. Bertino, *J. Magn. Magn. Mater.*, 2010, **322**, 2199

[69] X. Batlle, M. Garc□a del Muro, J. Tejada, H. Pfeiffer, P. Görnert, E. Sinn, *J. Appl. Phys.*,1993, **74**, 3333

[70] Y. Zhang, Y. Liu, C. Fei, Z. Yang, Z. Lu, R. Xiong, D. Yin, and J. Shi, *J. Appl. Phys.*, 2010, **108**, 084312

[71] R. Skomski, *J. Magn. Magn. Mater.*, 2004, **272**, 1476

[72] E. L. Verde, G. T. Landi, M. S. Carrião, A. L. Drummond, J. A. Gomes, E. D. Vieira, M. H. Sousa, and A. F. Bakuzis, *AIP Adv.*, 2012, **2**, 032120

[73] R. Skomski, *J. Phys.: Condens. Matter*, 2003, **15**, R841

[74] R. Aquino, J. Depeyrot, M. H Sousa, F. A. Tourinho, E. Dubois and R. Perzynski, *Phys. Rev. B*, 2005, **72**, 184435

[75] G. Burns, in *Solid State Physics Academic*, New York, 1985, pp. 578

[76] J. Y. Kim, T. Y. Koo, J. H. Park, *Phys. Rev. Lett.*, 2006, **96**, 047205

[77] T. Arima, D. Higashiyama, Y. Kaneko, J. P. He, T. Goto, S. Miyasaka, T. Kimura, K. Oikawa, T. Kamiyama, R. Kumai, Y. Tokura, *Phys. Rev. B*, 2004, **70**, 064426

[78] L. M. García, J. Chaboy, F. Bartolomé, J. B. Goedkoop, *Phys. Rev. Lett.*, 2000, **85**, 429

[79] S. Chikazumi, in *Physics of Magnetism*, Wiley, New York, 1964, pp. 283

[80] E. C. Stoner, E. P. Wohlfarth, *Philos. Trans. R. Soc*., 1948, **A240**, 559; reprinted in *IEEE. Trans. Magn.*, 1991, **27**, 3475.

Table 1. XRD results and Rietveld refinement parameters for $CuFe_2O_4$ sample (NP and NS).

Formula: $CuFe_2O_4$; **Crystal system:** FCC; **Space Group:** $Fd\bar{3}m$;	**Samples**	
	NP	**NS**
Scherrer's size, $<d_{311}>$/ nm	9	14
Lattice parameter, *a*/Å as calculated using eqn. 2	8.4031	8.3745
Refinement Parameters		
Lattice parameter, *a*/Å	8.41(2)	8.38(5)
Isotropic size, $<d_{iso}>$ /nm	10.4(4)	114.6(1)
Oxygen parameter, u	0.385(5)	0.3856(9)
Agreement factors		
[a]R_w	6.956	1.379

[b] R_{exp}	5.887	1.184
[c] GOF	1.18	1.16

Values within the parenthesis signify the estimated standard deviation, [a] $R_w = [\ \frac{\sum_i w_i(I_o - I_c)^2}{\sum_i w_i {I_o}^2}\ ]^{1/2}$, [b] $R_{exp} = [\frac{(N-P)}{\sum_i w_i I_o^2}]^2$, [c] Goodness of fit, $GOF = \frac{R_w}{R_{exp}}$,

Table 2. Average tetrahedral (A) and octahedral (B) interionic bond distances (see supplementary information).

Parameters (Å)	**Sample**	
	NP	**NS**
R_{OA}	1.9664	1.9681
R_{OB}	2.0184	2.0061
d_{AE}	3.2088	3.2140
d_{BE}	2.7378	2.7115
d_{BEU}	2.9780	2.9680
r_A	0.6464	0.6481
r_B	0.6984	0.6861

Table 3. ^{57}Fe Mössbauer parameters for $CuFe_2O_4$ NP and NS sample at 300 K.

Samples	**Isomer shift (δ in mm/s)**	**Quadrupole splitting (ΔE_Q in mm/s)**	**Average Hyperfine field (B_{Hf} in Tesla)**	**Area fraction (%)**

NP	Doublet	0.45	0.73	-	33.0
	Sextet	0.24	-	49.7	67.0
NS	Doublet	0.24	0.40	-	4.7
	Sextet 1 (A)	0.43	0.002	48.8	39.3
	Sextet 2 (B)	0.30	0.041	51.1	56.0

Table 4. Saturation magnetization (M_S), reduced remanent magnetization (M_R/M_S), coercive field (H_C) as determined at 5 K and 300 K for $CuFe_2O_4$ NP and NS samples.

Temperature	**M_S (emu/g)**		**M_R/M_S**		**H_C (Oe)**	
	NP	**NS**	**NP**	**NS**	**NP**	**NS**
5 K	7.97	7.53	0.5	1.0	956.5	456.2
300 K	1.04	5.28	0.2	0.7	294.9	546.7

Table 5. Parameters obtained by fitting the high-field $M(H)$ data to equation 4; goodness of fit (R^2), saturation magnetization (M_S), estimated magnetic anisotropy (K_E) using equation 5 and theoretical coercivity ($\gamma K_E/ M_S$), considering cubic anisotropy in NS sample ($\gamma = 0.64$).

Temperature (K)	***R^2***	***b***	***M_S* (emu/g)**	***K_E* (10^5 erg/cm^3)**	**$\gamma K_E/ M_S$ (Oe)**
5	0.991	0.002115	7.351 ± 0.381	0.325 ± 0.020	282.95
25	0.997	0.001757	7.561 ± 0.178	0.306 ± 0.031	259.01
50	0.999	0.000701	7.446 ± 0.151	0.190 ± 0.018	163.31

100	0.990	0.001381	7.181 ± 0.345	0.255 ± 0.016	227.27
200	0.993	0.005978	6.969 ± 0.604	0.520 ± 0.024	477.54
280	0.997	0.005298	5.213 ± 0.265	0.365 ± 0.018	446.57
300	0.998	0.005370	4.793 ± 0.512	0.340 ± 0.023	554.00

Figure captions

Figure 1. Experimental (blue circles) and computed (red solid line) X-ray powder diffraction patterns of $CuFe_2O_4$ samples: (a) NP and (b) NS. The difference pattern (black solid line) appears bellow.

Figure 2. FESEM images of (a) ~ 90 nm uniform spherical assembly of $CuFe_2O_4$ nanoparticles (NS) and (b) agglomerated $CuFe_2O_4$ nanoparticles (NP). The inset in (a) illustrates high magnification FESEM image of NS sample.

Figure 3. TEM and HRTEM images of $CuFe_2O_4$ NP sample (panels a and b, respectively) and $CuFe_2O_4$ NS sample (panels c and d, respectively). Inset in panel a shows particle size distribution obtained by averaging the sizes of approx. 100 nanoparticles in different TEM images.

Figure 4. (a) IR and (b) Raman spectra of $CuFe_2O_4$ NP and NS sample.

Figure 5. ^{57}Fe Mössbauer spectra recorded at 300 K of $CuFe_2O_4$ (a) NP and (b) NS sample; symbols represent the experimental data and the continuous lines correspond to the NORMOS fits.

Figure 6. Temperature dependence of FC and ZFC magnetization under a field of 100 Oe for $CuFe_2O_4$ NP and NS sample.

Figure 7. Field-dependent magnetization of $CuFe_2O_4$ NP and NS sample at (a) 5 K and (b) 300 K (enlarged loop areas near zero magnetic field); inset in panels a and b show the magnetization curves in the field range ± 3.5×10^4 Oe at 5 K and 300 K, respectively.

Figure 8. Temperature dependence of saturation magnetization (M_S) for $CuFe_2O_4$ NP and NS sample.

Figure 9. Temperature dependence of (a) coercive field (H_C) and (b) reduced remanant magnetization (M_R/M_S) for $CuFe_2O_4$ NP and NS sample, inset in panel (a) shows Kneller's fit (equation 3) of H_C data for NP sample.

Figure 10. (a) Temperature dependence of saturation magnetization (M_S) as obtained by fitting the high-field $M(H)$ data to equation 4 and the estimated magnetic anisotropy (K_E) of $CuFe_2O_4$ NS sample using equation 5; (b) temperature dependence of experimental coercivity (H_C) and theoretical coercivity ($\gamma K_E/M_S$) considering cubic anisotropy ($\gamma = 0.64$) in the system.

Figure 11. Sketch of the magnetic easy axis orientation in $CuFe_2O_4$ (a) NP and (b) NS sample.

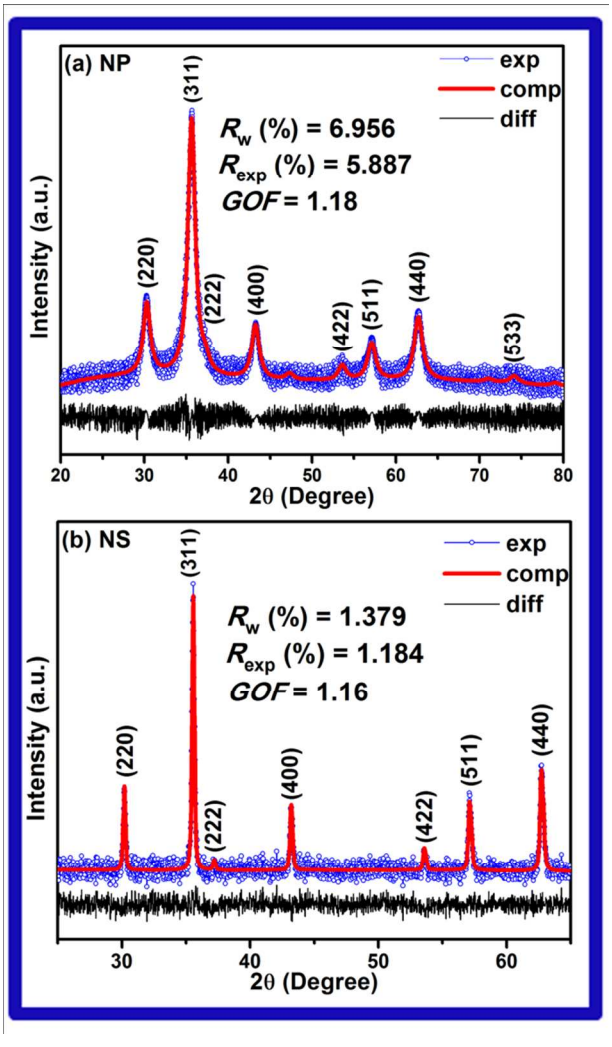

Figure 1

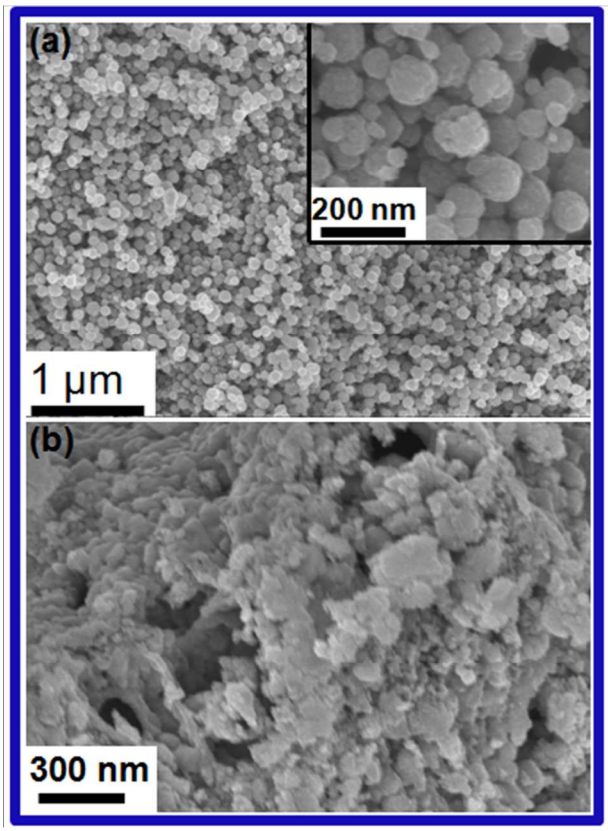

Figure 2

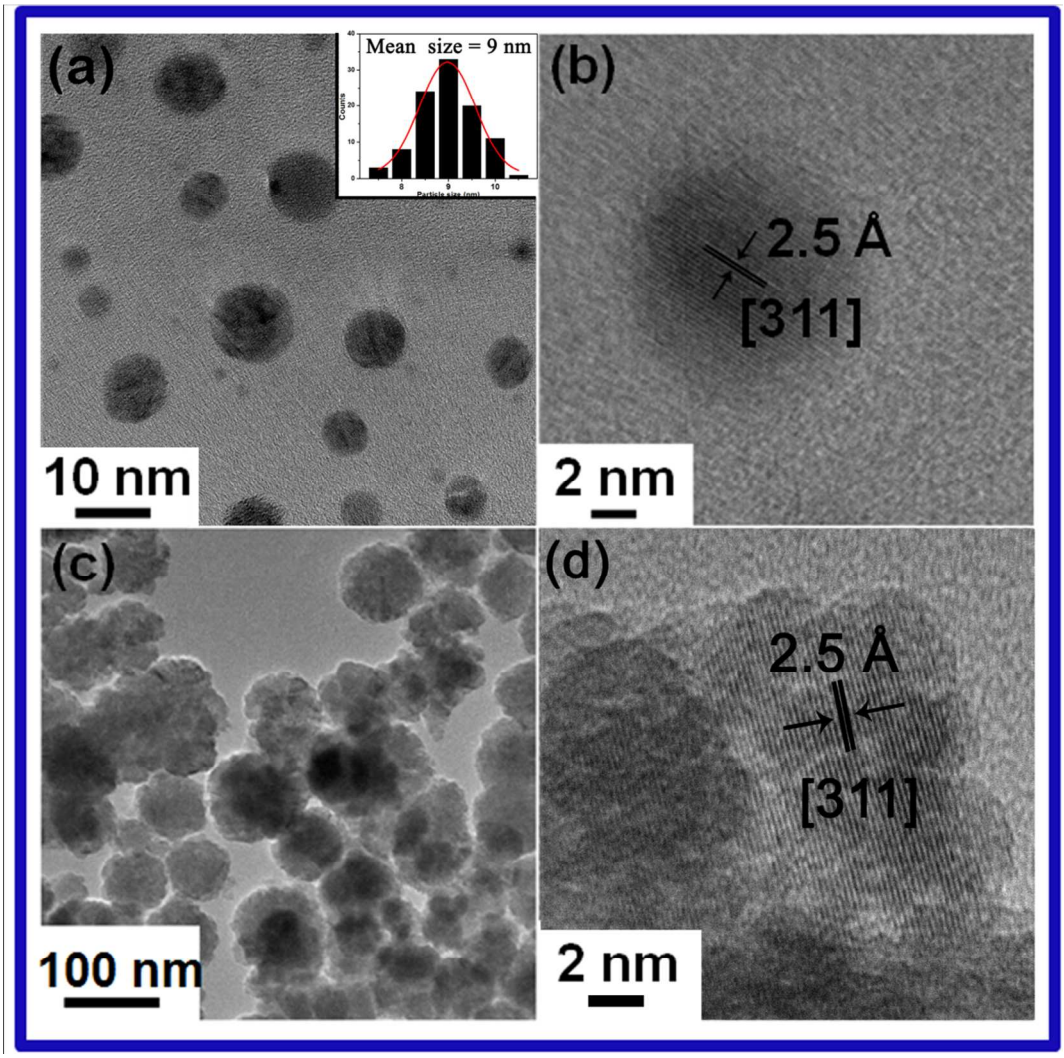

Figure 3

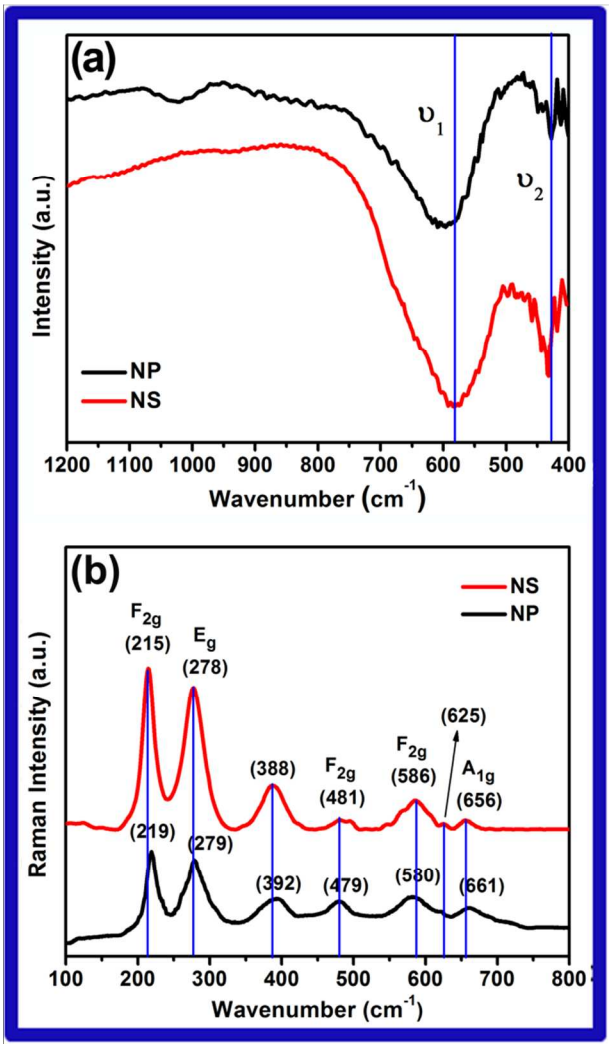

Figure 4

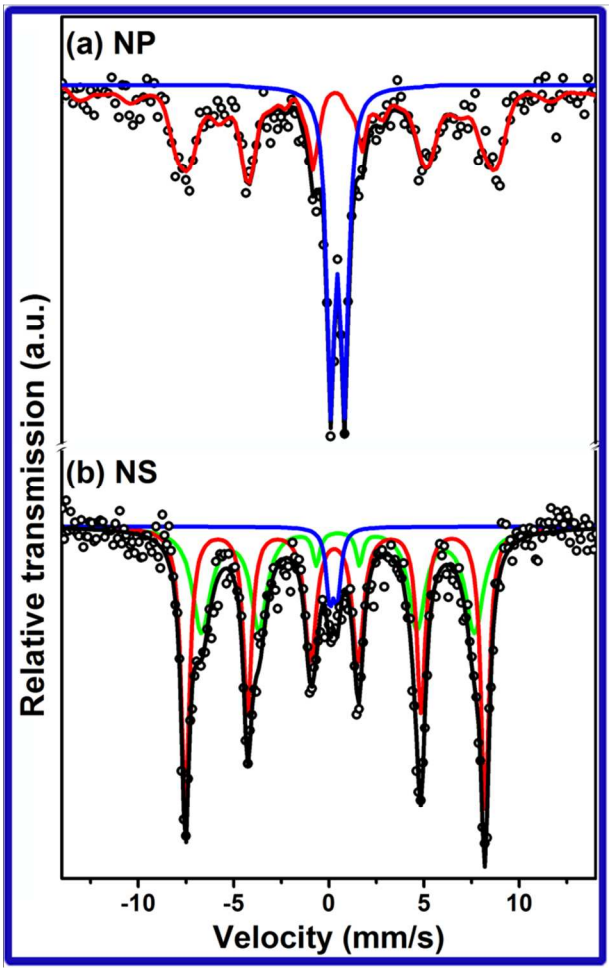

Figure 5

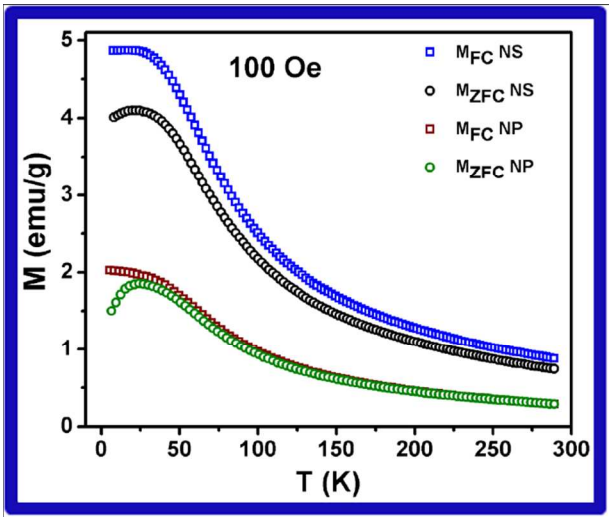

Figure 6

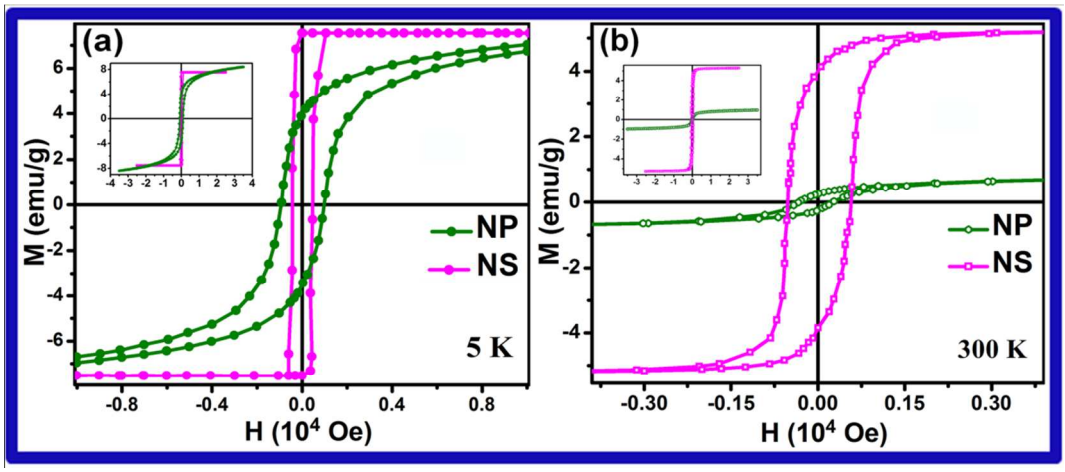

Figure 7

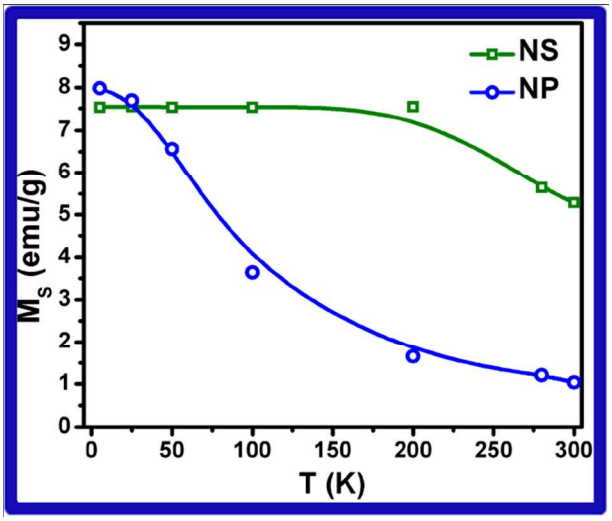

Figure 8

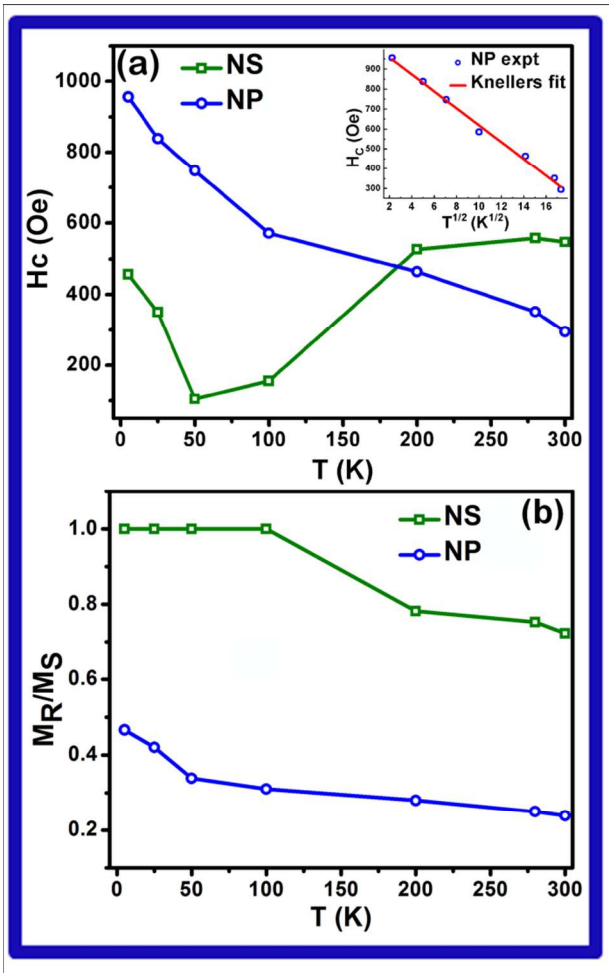

Figure 9

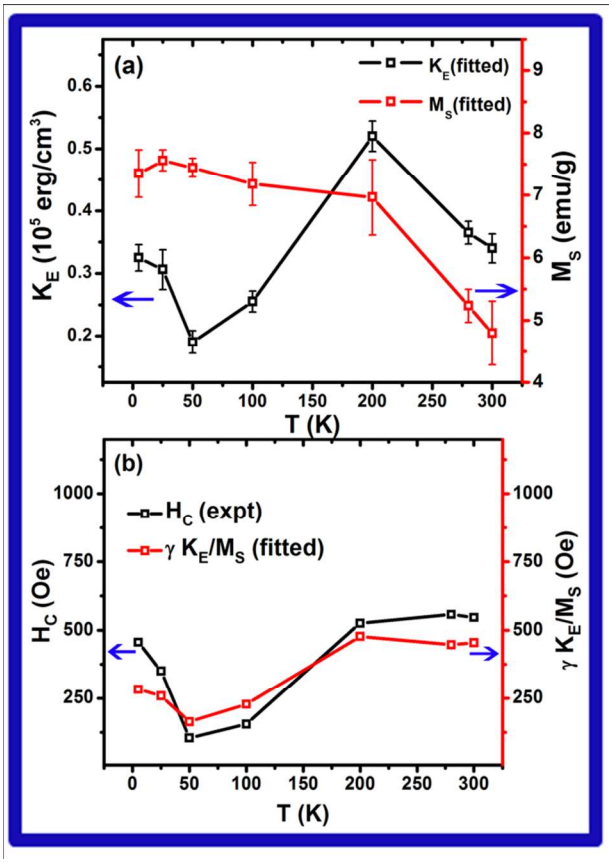

Figure 10

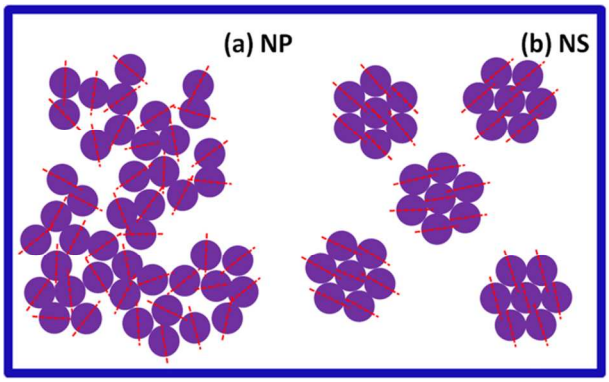

Figure 11

Table of contents for

Influence of spherical assembly of copper ferrite nanoparticles on magnetic properties: Orientation of magnetic easy axis

Biplab K. Chatterjee, Kaustav Bhattacharjee, Abhishek Dey, Chandan K. Ghosh and Kalyan K. Chattopadhyay*

Graphical contents

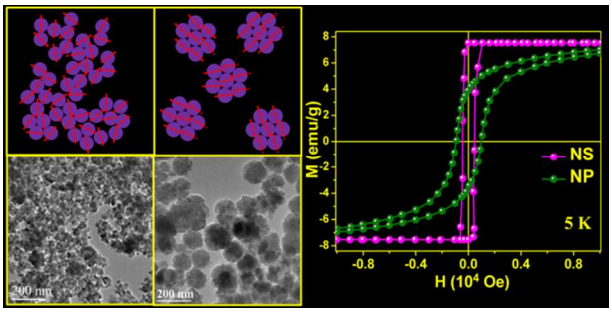

The spherical arrangement of $CuFe_2O_4$ nanoparticles (NS) stimulate a high degree of alignment of magnetic easy axis as compared to randomly oriented $CuFe_2O_4$ nanoparticles (NP) leading to an increase in reduced remanence ($M_R/M_S \sim 0.5$ to 1) and straightened hysteresis loop.

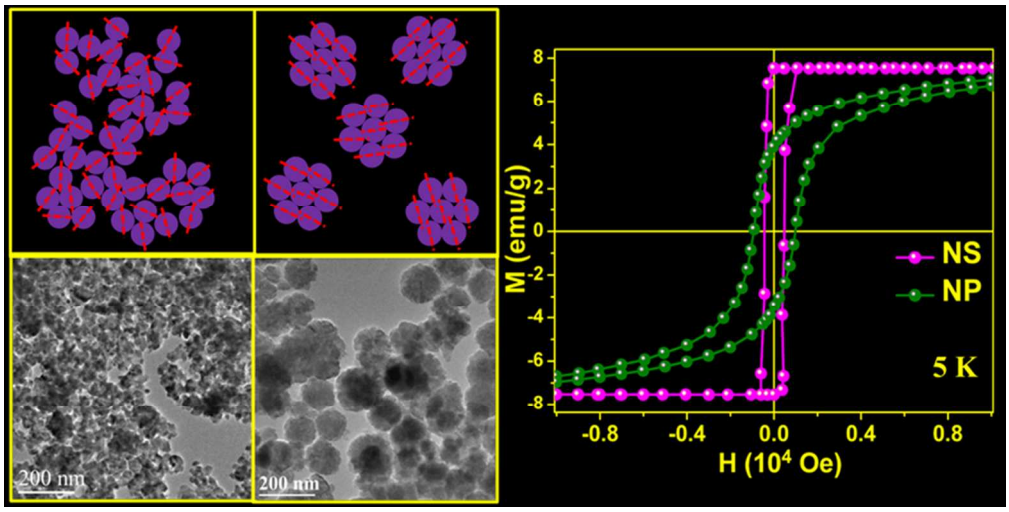

40x20mm (600 x 600 DPI)